A Structure Modality Enhanced Multimodal Imaging Method for Electrical Impedance Tomography Pressure Distribution Measurement

Huaijin Chen, Zhanwei Wang, Kevin Langlois, Tom Verstraten, Bram Vanderborght

***Abstract*—Electrical Impedance Tomography (EIT) based pressure distribution sensors have the advantages of a simple structure and the ability to continuously measure pressure over a large area, making it a promising solution for large scale artificial robotic skin. However, achieving high spatial resolution reconstruction of pressure distribution with EIT pressure sensors is challenging, because the positions, sizes, and magnitudes of pressure of the compressed areas are deeply coupled and mutually influenced in the EIT reconstructed results. To address this issue, a novel multimodal EIT pressure distribution measurement method is proposed. In this method, a structure modality EIT pressure sensor is designed to provide independent position and size information of the compressed areas to complement the pressure distribution measured using a normal EIT pressure sensor. A multimodal Convolutional Neural Network (CNN) was designed to fuse the multimodal EIT sensors. The simulations and experiments demonstrate that the proposed multimodal EIT sensor outperforms the regular single modality EIT sensor.**

***Index Terms*—Electrical Impedance Tomography (EIT), multimodal sensor fusion, pressure distribution measurement**

I. INTRODUCTION

Pressure distribution sensors are important to ensure safe interaction between environments and robots. This kind of sensor (also referred to as artificial robotic skin) is supposed to be flexible, as large as it can cover the entire robot, and suitable for various curved surfaces [1]. As for the pressure sensor that is composed of discrete pressure sensors array, it is not easy to achieve the requirement, because of its complicated inner cables and structures [2].

Electrical Impedance Tomography (EIT) based pressure sensor is a promising solution for the requirements above. Determined by the principle of EIT, the EIT pressure sensor has features of simple structure [3], capabilities of measuring the pressure distribution over a large area and curved surfaces. More importantly, the EIT pressure sensor can achieve spatial continuous pressure distribution measurement [4]. A more thorough comparison between the EIT pressure sensors and other types of pressure sensors can be found in the review paper [5].

Nowadays, different kinds of EIT pressure sensors have been developed. A stretchable EIT sensor was developed by H. Alirezaei et al., and its flexibility is validated with a humanoid face and elbow joint [6]. D. Silvera-Tawil et al. proposed a social touch emotions interpretation method based on an EIT tactile sensor embedded artificial limb [7, 8]. Y. Zhang et al. proposed an EIT tactile sensing method for very large-scale areas and complex curved surfaces [9]. K. Park et al. developed an EIT pressure sensor for an industrial robotic arm [2]. N. Biasi et al. developed an insole-shaped EIT sensor prototype, in which, the sensing area has an irregular boundary shape [10]. In our former work, an EIT sensor embedded Physical Human Robot Interface (PHRI) was developed to measure the interaction compression between PHRI and the human body [11]. The potential and flexibility of EIT sensors have been demonstrated in the studies above.

However, the sensitivity of EIT sensors is not evenly distributed, which means that the measurement of pressure magnitude is affected by the position of the compressed area. Meanwhile, the size of the compressed area also impacts the pressure magnitude measurement, and vice versa. Hence, accurately reconstructing pressure distribution with EIT sensor is highly challenging. Extra methods are required to rectify the reconstruction result of the conventional EIT algorithms, especially for pressure magnitude estimation. One typical solution is dividing the sensing region into several discrete sections and manually calibrating them one by one [12, 13]. The other proposed sensitivity rectify method is based on the Jacobian matrix (also known as sensitive matrix) in the EIT inverse problem [14]. However, these studies are mainly aimed at the cases of single compression area with constant size, and lack studies on complex situations of varying sizes and numbers of compressed areas.

Recently, single modality Artificial Intelligence (AI) has been applied in the EIT reconstruction process and outperformed conventional algorithms. However, including our previous work [11], Most studies [2, 10, 15, 16] mainly focus on reconstructing the position, size, and shape (referred to as structure) of the compressed areas, while the studies on pressure magnitude measurement are limited. In [17], a single modality AI is used but only for segmenting the compressed areas from the background, then an extra manual calibration is applied for pressure magnitude estimation, which is cumbersome. Hence, a method that can directly reconstruct

This work is supported in part by the China Scholarship Council (CSC) under NO. 202106830032 and NO. 202006080010; the Wetenschappelijk Onderzoek (FWO) under grant 1258523N (Corresponding author: Huaijin Chen).

H. Chen, Z. Wang, K. Langlois, and B. Vanderborght are with Brubotics, Vrije Universiteit Brussel and imec, Pleinlaan 2, 1050 Brussels, Belgium (e-mail: Chen.Huaijin@vub.be; Zhanwei.Wang@vub.be; Kevin.Langlois@vub.be; bram.vanderborght@vub.be).

T. Verstraten is with Brubotics, Vrije Universiteit Brussel and Flanders Make, Pleinlaan 2, 1050 Brussels, Belgium (tom.verstraten@vub.be).

the positions, sizes, and pressure magnitudes of compressed areas is needed.

To address the issue, we propose a novel dual-modality EIT pressure sensing method based on multimodal AI and sensor fusion. The main idea of multimodal sensor fusion is extracting and fusing features from different sensing modalities to complement each other [18, 19]. In the case of conventional single modality EIT sensor, the magnitude and structure of the compressed area are mutually influenced, then adding an independent structural modality to provide complementary information. Researchers in the medical field explored using other tomography methods such as Magnetic Resonance Imaging (MRI), optical method, and Computed Tomography (CT) [20-22] to provide extra structure information to complement EIT. However, the methods above are not available for the EIT pressure sensor because the devices are too bulky, and an efficient structure modality sensor is needed for the EIT pressure sensor.

To address this issue, a multimodal EIT pressure sensor is proposed. It is not only composed of a regular EIT pressure sensor that acquires the magnitude of the compressed areas, but also a specifically designed structure modality EIT pressure sensor. This additional modality acquires extra structure information of the compressed areas. To achieve this function, the mechanism of saturation state of piezoresistive materials is employed to extract the position and geometry of the compressed areas without being affected by varying pressure magnitudes.

A dual-modality Convolutional Neural Network (referred to as multimodal CNN) enhanced conventional algorithms is designed to fuse the information from two modality sensors and reconstruct the pressure distribution. This AI enhance conventional algorithms strategy is also referred to as "two-step method". It is robust against noise in the studies of single modality EIT [23, 24], and it is deduced to remain the same feature in multimodal CNN. In this method, the data acquired from magnitude modality EIT sensor is first process using a conventional algorithm (Tikhonov regularization is selected, based on our previous study [11]) to obtain a preliminary reconstruction and then input into magnitude modality of the multimodal CNN. For structure modality, the Parametric Level Set (PLS) method [25] is adopted to bridge the structure modality sensor and the multimodal CNN because of its excellent performance in structure reconstruction. On the other hand, the proposed structural EIT sensor simplifies the conductivities as two phases, which are compressed and uncompressed areas regardless of the number of compressed areas and pressure amplitudes. This feature satisfies the requirement of the PLS method that the number of conductivity phases is needed as prior, where the regular EIT pressure sensors are not suitable.

The innovation of this paper lies in the proposal of a multimodal EIT sensor featuring a specially designed structure modality. It facilitates the utilization of a multimodal sensor fusion approach for EIT pressure measurement, thereby enhancing performance. The structure of this paper is as follows: In section 2, the proposed multimodal EIT sensor is presented and the mechanism of achieving multimodal is illustrated. In section 3, the multimodal AI enhanced EIT reconstruction method is explained. In section 4, the simulation study results of the algorithm are presented. In section 5, the experimental validation of the multimodal EIT sensor is presented.

II. DEVELOPMENT OF MULTIMODAL EIT PRESSURE SENSOR

The architecture and mechanism of the multimodal EIT sensors are illustrated in this section. The sensor is mainly composed of two isolated EIT sensors that are stacked, as shown in Fig. 1 (a). The top sensor measures pressure magnitude distribution. It is composed of Velostat conductive film and a conductive cloth patches matrix. Velostat is the main body of the sensor, and 16 square electrodes (made of copper tape) are mounted on the edges evenly. The shape of the sensor is a square with a length of $l_{sensor} = 150\,mm$. The length of the electrode is $l_e = 6\,mm$, and the distance between each two electrodes is $d_e = 36\,mm$. The flexible padding is for retaining conductive cloth patches matrix, and the spacer mesh is placed between Velostat and conductive cloth patches matrix. These two parts are both 3D printed with TPU-60 flexible filament. The sensitivity of the sensor can be controlled by adjusting the hardness of the flexible padding and the sparsity of the spacer mesh.

The mechanism of the EIT sensor is that the conductivity of Velostat is lower than the conductive cloth. When they are forced to contact, the current that is injected through the electrodes into the Velostat partially flows through the low-resistance conductive cloth. This is how an increased pressure will lead to an equivalently increased conductivity. More details of the mechanism can be found in this study [26].

The structure modality sensor is placed under the magnitude modality sensor. The settings of the two sensors are the same, including the geometry of the Velostat film, the conductive cloth patches, and the arrangement of the electrodes. Differently, there is no spacer mesh in the structure modality sensor, which makes it more sensitive to pressure. The two EIT sensors are electrically isolated by a non-conductive layer. A top frame and a middle frame are used to compress electrodes against two EIT sensors respectively to ensure stable contact. The sensing area is a square area that is not covered by the top frame, and its area is $(150 - 2 \times 6)^2 = 19044\,mm^2$.

The operating principle of the multimodal sensor is shown in Fig. 1 (b). Both EIT sensors are piezoresistive, and the local conductivity changes according to the pressure that is applied, but the sensitivity of the two sensors is different. The structure modality sensor is highly sensitive, and it saturates quickly under lower pressure because the spacer mesh is not used in this sensor. The conductive cloth patches easily make full contact with the Velostat layer. At this point, the structure modality sensor is no longer sensitive to the changes of pressure. Hence, the output of the structure modality sensor is a binary quantity of "compressed" and "uncompressed", which only preserves the geometric information of the compressed areas. However, the magnitude modality sensor has lower sensitivity due to the spacer mesh and its response still depends on the magnitude of the pressure.

To acquire data from the proposed multimodal EIT sensor, a dual-channel EIT data acquisition device is modified from our previous work [11]. The main improvement is expanding data acquisition channels to two channels. In programming design, multi-threads technology is adopted to accelerate the data acquisition process and ensure the synchronization between two modalities. Adjacent current injection protocol [27] is used for both modalities. More details about the data acquisition device can be seen in Supplementary Material 1.

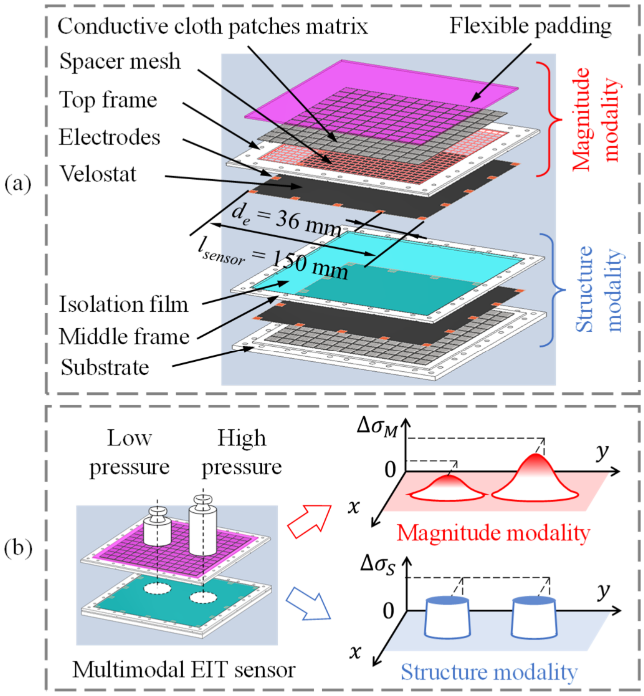

Fig. 1. The structure of the multimodal EIT pressure sensor (a) The 3D modal of the sensor. (b) Illustration of the mechanism of the multimodal sensor. As shown, the conductivity magnitude of magnitude modality sensor varies with different pressure, and that of structure modality sensor dose not, because the structure modality sensor works in the saturation state. It can provide more accurate geometric information of compressed areas then enhance magnitude modality sensor.

III. MULTIMODAL CNN IMAGING METHOD

In this section, a "two-step" multimodal AI enhanced EIT reconstruction method is presented for fusing two modality EIT sensors. Firstly, applying conductivity distribution reconstruction algorithms to the magnitude modality sensor to acquire a preliminary pressure distribution estimation with the pressure magnitude information. For this purpose, the Tikhonov regularization is adopted. Then the shape reconstruction algorithm of the PLS method is applied to the structure modality sensor. This combination reconstructs more accurate images of the position and geometry of the compressed areas to complement the magnitude modality. Finally, a multimodal CNN is used for sensor fusion to achieve better reconstruction.

A. EIT principle

The time differential EIT inverse problem is explained firstly, and both magnitude and structure EIT modality sensors are submitted to this theory. It is reconstructing the perturbation of the conductivity distribution inside a given domain Ω. The stimulation current I is injected through the border of Ω to form an electrical field. When the EIT pressure sensor is being compressed, the local conductivity of the compressed area varies, as Ω^+ shown in Fig. 2, and Γ is its boundary. The voltage V on the boundary of Ω varies accordingly and is measured to reconstruct Ω^+. Ω^- represents the conductivity remaining area, which is referred to as background.

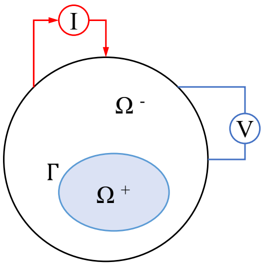

Fig. 2. Illustration of EIT principle. Ω^+ is the conductivity varying area, and Ω^- represents the conductivity remaining area. Stimulation current I is injected to electrical field and voltage V is measured to reconstruct Ω^+.

Using the Finite Element Method (FEM), the EIT problem is linearized as:

$$\Delta\boldsymbol{V} \approx J\Delta\boldsymbol{\sigma} \tag{1}$$

where $\Delta\boldsymbol{\sigma} \in \mathbb{R}^{N\times1}$ is the vector of internal conductivity perturbation inside Ω , $\Delta\boldsymbol{V} \in \mathbb{R}^{M\times1} (M \ll N)$ is its corresponding boundary voltage variation vector, and $J \in \mathbb{R}^{M\times N}$ is the Jacobian matrix, as:

$$J_{ij}(k) = \frac{\partial \boldsymbol{V}_{ij}}{\partial \boldsymbol{\sigma}_k} = -\int_{pixel\ k}^{\square} \nabla\boldsymbol{u}(I_i)\cdot\nabla\boldsymbol{u}(I_j)dV \tag{2}$$

where $\nabla\boldsymbol{u}(I_i)$ and $\nabla\boldsymbol{u}(I_j)$ are gradients of the potential fields $\boldsymbol{u}$ when the current is injected into the i^{th} and j^{th} electrodes pairs, respectively [28].

When the shape of the sensor and current injection protocol is set, the sensitive matrix is determined. Then, to intuitively show the unevenness of the sensitivity distribution of the EIT sensor, the method in [29, 30] is adopted. In this method, the sensitivity matrix is visualized as sensitive maps. The sensitivity maps are shown in Supplementary Material 2. As shown, the sensitivity is highly uneven, and the center area of the sensor is always with low sensitivity.

B. Conventional algorithms for "two-step" method

1) **Tikhonov regularization**

Based on equation (1), the conductivity variation distribution of $\Delta\hat{\boldsymbol{\sigma}}_M$ in magnitude EIT sensor is estimated by solving equation (3) as follow:

$$\Delta\hat{\boldsymbol{\sigma}}_M = \arg min(\|J\Delta\boldsymbol{\sigma}_M - \Delta\boldsymbol{V}_M\|_2^2 + \lambda\|\mathrm{L}\Delta\boldsymbol{\sigma}_M\|_2^2) \tag{3}$$

where subscript M indicates that the data is sourced from the magnitude modality sensor, Because the Jacobian matrix J is ill-posed, Tikhonov regularization is adopted to obtain stable solutions [31]. Where λ is the regularization parameter, and L is regularization matrix. This paper uses the non-iteration form of the standard Tikhonov regularization, so matrix L is used as identity matrix I. The equation is written as:

$$\Delta\hat{\boldsymbol{\sigma}}_M = (J^TJ + \lambda I)^{-1}J^T\Delta\boldsymbol{V}_M \qquad (4)$$

2) **Parametric Level Set method**

The Parametric Level Set (PLS) method is a shape reconstruction method and outperforms direct conductivity distribution recovering methods such as Tikhonov regularization in the aspect of geometry reconstruction of conductivity varying areas. So, its geometric reconstruction result of the compressed areas is more suitable for the structure modality of the multimodal network. Limited by the length, only the basic ideology of the PLS method and how the PLS integrated with our structure modality EIT sensor are introduced in this part, and more details of the PLS method can be found in [25, 32-34].

The main idea of the PLS method assumes that the internal conductivity of the given domain is composed of a few separate areas with piece-wise constant conductivities, and each piece is referred to as one phase. Instead of directly recovering the conductivity distribution by pixels, this shape reconstruction method aims to estimate the constant values of conductivities and boundaries of these areas.

With the Level Set Function (LSF) of the PLS method as shown in equation (5):

$$\begin{cases} f(x) > 0 & \forall x \in \Omega^+, \\ f(x) = 0 & \forall x \in \Gamma, \\ f(x) < 0 & \forall x \in \Omega^-. \end{cases} \qquad (5)$$

where the conductivity distribution $\Delta\sigma_S$ of the given domain Ω in Fig. 2 is expressed:

$$\Delta\sigma_S(x) = \Delta\sigma_{S0}\Big(1 - H\big(f(x)\big)\Big) + \Delta\sigma_{S1}H\big(f(x)\big) \qquad (6)$$

where the subscript S indicates structure modality, $\Delta\sigma_{S0}$ is background conductivity, $\Delta\sigma_{S1}$ is that of the conductivity varying area Ω^+. $H(y)$ is the Heaviside function, where $H(y) = 0,\ y < 0$ and $H(y) = 1,\ y \geq 0$. In this paper, the Gaussian Radial Basis Functions (Gaussian RBFs) is used as function $f(x)$:

$$f(x) = \sum_{i=1}^{N} \mu_i\, p_i(x) \qquad (7)$$

where $p_i(x)$ is the i^{th} RBF kernel, μ_i is the weight of the it, $i \in [1,2,\cdots,N]$. The equation (1) is then rewritten as:

$$\Delta\boldsymbol{V}_S \approx J\Delta\boldsymbol{\sigma}_S(\boldsymbol{\mu}, \Delta\sigma_{S0}, \Delta\sigma_{S1}) \qquad (8)$$

and the shape reconstruction of the conductivity varying areas is solving the minimization problem:

$$[\hat{\boldsymbol{\mu}}, \Delta\hat{\boldsymbol{\sigma}}_{S0}, \Delta\hat{\boldsymbol{\sigma}}_{S1}] = \arg\min\left(\|J\Delta\boldsymbol{\sigma}_S(\boldsymbol{\mu}, \Delta\sigma_{S0}, \Delta\sigma_{S1}) - \Delta\boldsymbol{V}_S\|_2^2\right) \qquad (9)$$

Correctly assuming the number of phases is needed in the PLS method. The equations above illustrate the cases of two phases imaging, where two piece-wise constant conductivities of $\Delta\sigma_{S0}$ and $\Delta\sigma_{S1}$ are assumed in PLS modeling. According to the study of multiphase PLS [35], underestimating the number of phases leads to errors in the reconstruction of the image. Hence, the PLS method is not able to extract structural information of the compressed area from a regular EIT pressure sensor (neither could our previously developed sensor [11]).

In the proposed structure modality EIT sensor, the conductivity variation of the compressed areas is constant under different pressures. Therefore, regardless how many areas are being compressed, the conductivity of the sensor can always be expressed by two phases, enabling the PLS method in structural reconstruction of the compressed areas.

C. Multimodal CNN

1) **Architecture**

The architecture of the multimodal CNN is shown in Fig. 3 (a), where the red dashed line box represents the magnitude modality. The vector of $\Delta\boldsymbol{V}_M$ is voltage data from magnitude modality sensor (adjacent current injection protocol is used in this paper, so 16 electrodes provide 208 voltage data), and converted by Tikhonov regularization into the preliminary estimation of the conductivity distribution variation of $\Delta\hat{\sigma}_M$. Before inputting feature extractor 1 for magnitude modality, a two steps pre-processing is applied to the $\Delta\hat{\sigma}_M$. First is negative value truncation, then is global 0-1 normalization that is schematically shown in Fig. 3 (b). The curves in Fig. 3 (b) with different colors represent different frames of data, σ_{ij}^{max} represent the maximum value of all the elements in all input frames. $i \in [1,2,\cdots,N]$ is the i^{th} frame in all N frames of input, $j \in [1,2,\cdots,M]$ is the j^{th} element in each frame.

The $\Delta\hat{\sigma}_M$ is then input into feature extractor 1, which has a typical CNN structure. As shown in Fig. 3 (d), it contains sixteen CNN blocks and each of them is composed of a 3×3 convolution layer, a Batch Normalization (BN) layer, and an Exponential Linear Unit (ELU) layer. It also contains five pooling layers for down sampling, and except for the last average pooling layer, the others are max pooling layers. The output of the CNN feature extractor is then flattened into a 1×4096 vector.

The blue dashed line box in Fig. 3 (a) represents the structure modality of the model, where the input is voltage data $\Delta\boldsymbol{V}_S$ from the structure modality sensor, and the current injection protocol is also the adjacent protocol. The PLS method is adopted for preliminary structural estimation of the conductivity variation $\Delta\hat{\sigma}_S$ instead of Tikhonov regularization. The data flow of the structure modality is similar to that of the magnitude modality, and the CNN feature extractor 2 is the same as the feature extractor 1 shown in Fig. 3 (d). In this modality, instance 0-1 normalization is used to process preliminary results of the PLS rather than global 0-1 normalization in magnitude modality. The schematic of the instance 0-1 normalization is shown in Fig. 3 (c), where σ_i^{max} represent the maximum value of the i^{th} frame in all N frames of input. After the processing in structure modality, the other 1×4096 vector is obtained.

The output vector of each modality is concatenated to form a 1×8192 vector and processed by two Fully Connected (FC) blocks. As shown in Fig. 3 (a), each FC block contains an FC layer, a BN layer, and a Rectified Linear Unit (ReLU) layer. After reshaping into a 51×51 matrix, 2D Gaussian filtering with a standard deviation of $\sigma = 1$ is applied to the output of $\Delta\hat{\sigma}$ to eliminate potential discrete noise points. The multimodal CNN is built with Pytorch 2.0, and its output type is regression with the Mean Squared Error (MSE) as loss function.

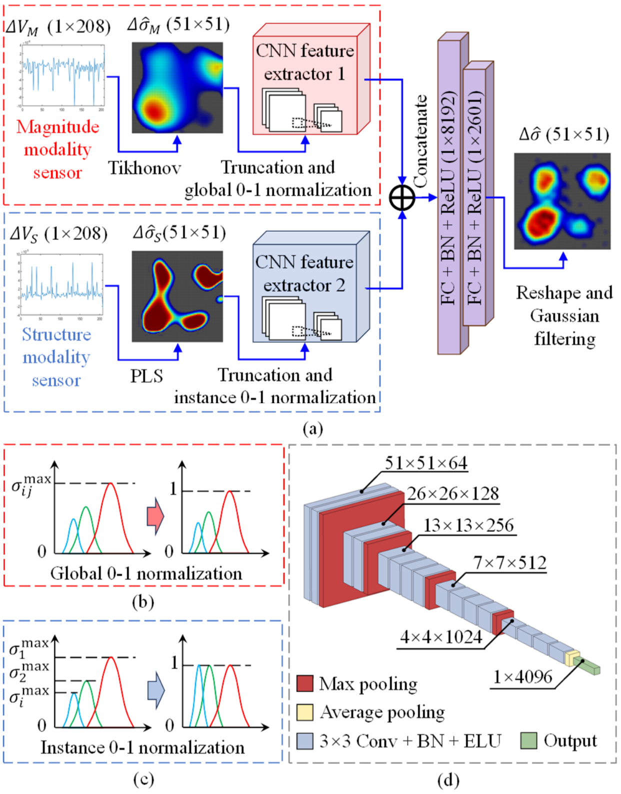

Fig. 3. Illustrations of the proposed multimodal CNN, (a) Illustrations of the data flow and the multimodal CNN structure, and (b) shows the schematic of global 0-1 normalization in magnitude modality, (c) shows the schematic of instance 0-1 normalization in structure modality, (d) shows the framework of CNN feature extractor, which is a universal model for both magnitude and structure modalities.

2) Training strategy

Since it is difficult to get enough training data from experimental setups for AI model training, simulation data were acquired with FEM for training. For the multimodal CNN in this paper, one group of training data contains one frame of conductivity distribution ground truth and two frames of voltage data for magnitude modality and structure modality respectively, rather than one voltage in single modality networks. Hence, a specific training data acquisition method is needed, as shown in Fig. 4.

First, the conductivity distribution models of ground truth are generated with FEM simulation as target data for network training. In the models, the shape of conductivity varying areas is elliptical with random parameters (positions, major and minor axis) and piecewise constant inner conductivity. The areas do not overlap in the case of multiple areas. The conductivity of background is heuristically set as $1\ S/m$, and that of conductivity varying areas are set as random values between $0.95-0.75\ S/m$. The voltage data $\boldsymbol{\Delta V}_M$ are generated and processed with Tikhonov regularization for the magnitude input of the network.

Then the structure of the conductivity variation is extracted by replacing the conductivities of conductivity varying areas with a constant conductivity of $100\ S/m$, and maintaining the background conductivity. With this step, the new models only contain two kinds of conductivities, one of which is for background, and one is for conductivity varying areas. The voltage data $\boldsymbol{\Delta V}_S$ are generated with the new models, then input into the structure modality of the network after being preprocessed by the PLS method.

In total, 12000 groups of data were acquired in simulation, each of them contains a set of $\boldsymbol{\Delta V}_M$, $\boldsymbol{\Delta V}_S$ and the ground truth. 10000 groups were used as training data, equally split into groups of one, two, three, and four varying areas. The other 2000 groups were used as testing data, and the number of the groups that contain one, two, three, and four conductivity varying areas equals 500.

In the training process, no specific customized training strategy was added, as the adopted multimodal network is symmetric and balanced between modalities. Meanwhile, no artificial noise was added to the training and testing data set during training. The Adaptive Moment Estimation (ADAM) was selected as the solver, with a constant learning rate $lr = 1e^{-4}$. The training is performed for 200 epochs with a minibatch size of 128, and the training data shuffled in every epoch.

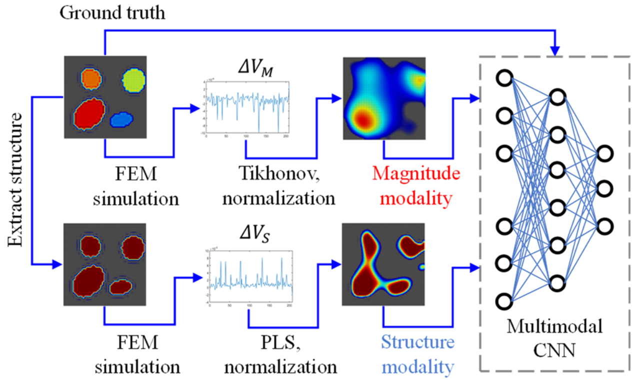

Fig. 4. The process of generating training data for multimodal CNN. Ground truth is generated first, and voltage data is generated in simulation then input into magnitude modality after preliminary processing using Tikhonov regularization. Then the structure of ground truth is extracted to generate voltage data for structure modality, where the preliminary processing method is PLS.

IV. SIMULATION VALIDATION

In this section, the multimodal CNN is verified with simulation tests, including the accuracy of imaging with different conductivity varying areas, and the robustness to the noise. For reference, the imaging results of the global 0-1 normalized Tikhonov regularization are given. Meanwhile, a single modality CNN is also presented for the ablation study. It is obtained by removing the structure modality of the multimodal CNN and only maintaining the magnitude modality. The other settings are the same as multimodal CNN, including training data and strategy.

In the tests, 400 groups of data are generated randomly, where the numbers of groups that contain one, two, three, and four conductivity varying areas are the same as 100. Meanwhile, white Gaussian noise with Signal-to-Noise Ratio (SNR) of 40 dB, 20 dB, and 10 dB was added to the data respectively, to verify the robustness of the algorithms.

A. Criteria

General EIT criteria are used in this test, the first one is Relative Image Error (RIE):

$$RIE = \frac{\|\hat{\sigma}_{pred}-\sigma_{gt}\|}{\|\sigma_{gt}\|} \tag{10}$$

where $\hat{\sigma}_{pred}$ is the reconstructed conductivity distribution and σ_{gt} is the ground truth of the conductivity distribution. The smaller the RIE, the more accurate the reconstruction results.

The second criterion is Imaging Correlation Coefficients (ICC):

$$ICC = \frac{(\hat{\sigma}_{pred}-\bar{\sigma}_{pred})\cdot(\sigma_{gt}-\bar{\sigma}_{gt})}{\|\hat{\sigma}_{pred}\|\cdot\|\sigma_{gt}\|} \tag{11}$$

where $\bar{\sigma}_{pred}$ is the average value of $\hat{\sigma}_{pred}$, and $\bar{\sigma}_{gt}$ is the average value of σ_{gt}. Larger ICC suggests accurate reconstruction.

B. Simulation results

Fig. 5. shows the simulation results. The first row is for RIE, and the second row is for ICC. Different columns are for different SNRs. The data in blue, red, and black are calculation results from multimodal CNN, single modality CNN, and Tikhonov regularization respectively. Overall, the lower RIE and higher ICC suggest that the results of the two CNN enhanced methods both outperform Tikhonov regularization. In the tests of single and two conductivity varying areas, multimodal CNN outperforms single modality CNN. When the number of areas increases to three, multimodal CNN barely has any advantage. In four conductive varying areas tests, the single modality CNN has more reconstruction accuracy. This trend is clearer when the SNR is higher, that is the data have less noise.

The figures for different noise levels suggest all methods are robust against noise. The RIE and ICC of all methods under $SNR = 40\ dB$ circumstance have barely any difference from that of noise free cases. Even when the noise reaches the level of $SNR = 10\ dB$, the reconstruction accuracy is only slightly decreased. The results confirm that the "two-step method" has high noise resistance, whether the AI model is single modality or multimodal. It is inferred that the robustness of the conventional algorithm is the key issue, which acts as the filter and increases the quality of the data that is input into the AI model, such as Tikhonov and PLS in this study.

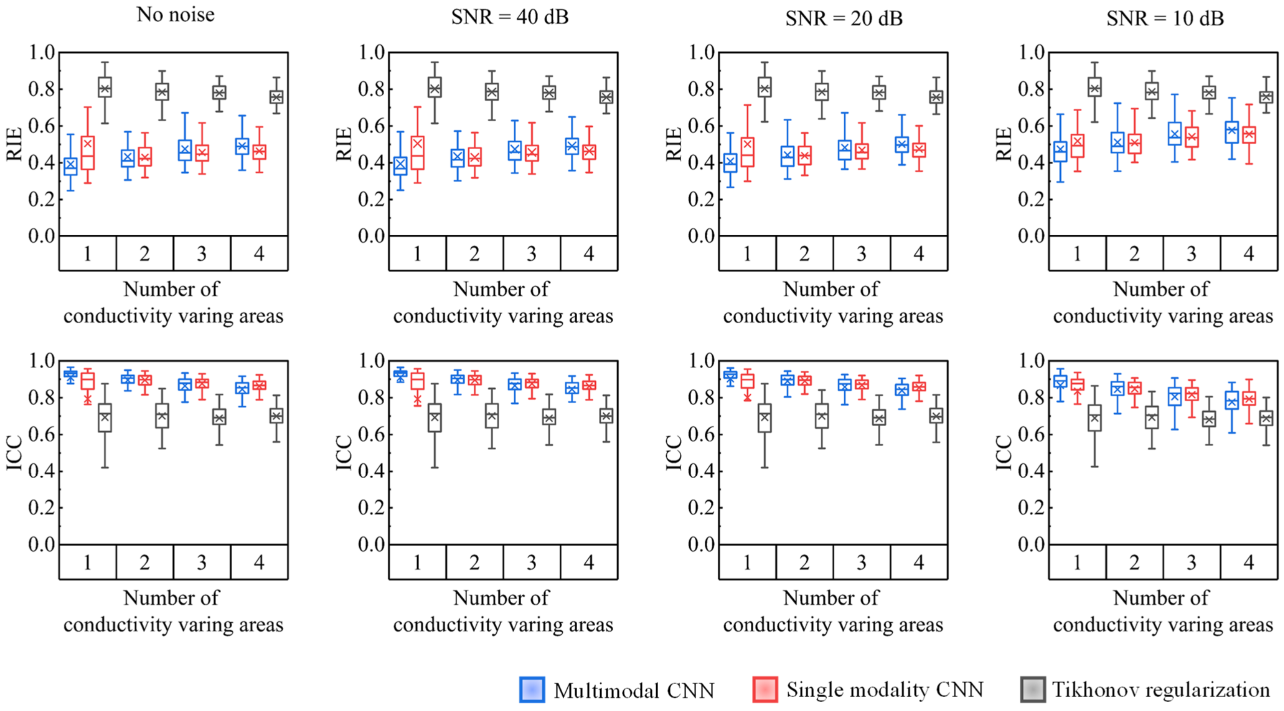

Fig. 5. The simulation results, figures in the first row are for RIE, and in the second row are ICC, different columns represent reconstruction results under different SNR. As shown, two AI enhanced methods outperform Tikhonov regularization, and multimodal CNN outperforms single modality CNN in the cases of reconstructing one and two conductive varying areas.

V. EXPERIMENTAL VALIDATION

In this section, the proposed multimodal EIT pressure distribution sensor is experimentally validated. The results of single and multiple areas compression tests are presented, including reconstructed pressure images and pressure magnitude estimation. Besides the reconstruction results of multimodal CNN, the results of single modality CNN and Tikhonov are also provided as comparison. Because the single modality CNN only uses the data from the magnitude modality of the multimodal sensor, which is a regular EIT pressure sensor, the comparison between multimodal CNN and single modality CNN also represents the comparison between the proposed multimodal sensor and the regular EIT pressure sensors.

A. Experiment platform

The experiment platform is shown in Fig. 6. The frame is made of aluminum plate profiles. A 7 × 7 threaded holes array is central symmetrically arranged on the top of the frame. It is used to position and install the modularized indenters, while also to cooperate with the compression handle and bolt of the indenter to apply pressure to the EIT sensor. The center of the matrix is aligned with the center of the frame. The distance between the holes is $D = 18\,mm$. Each indenter is equipped with an independent loadcell (type: FX293X-040B-0100-L) to monitor the pressure applied to the EIT sensor. The details about the experimental platform and the coordination alignment between the sensor and the experimental platform are shown in Supplementary Material 3.

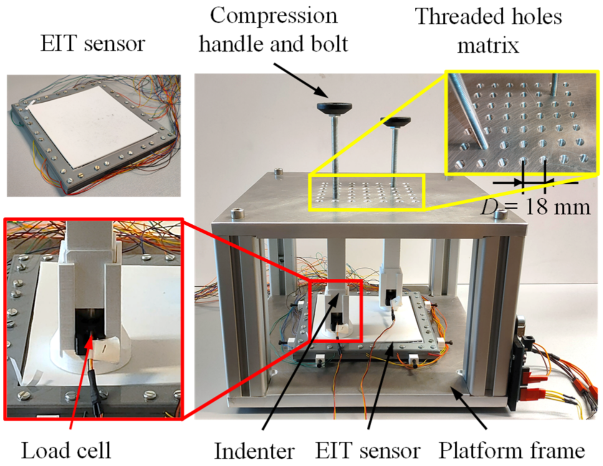

Fig. 6. The experiment platform. The indenter is modularized and can be positioned with threaded holes. Each indenter has an independent loadcell to monitor the pressure.

B. Multimodal EIT sensor mechanism validation

A test is designed to validate the mechanism of the proposed multimodal sensor. In this test, the raw voltage data were acquired from both sensor modalities when the pressure was applied, and the conductivity magnitude variation of both sensors was calculated with Tikhonov regularization. An indenter with diameter of $d = 30\,mm$ was used to apply pressure to the sensor. The pressure increases from 0 kPa to 200 kPa with a step of 20 kPa. To obtain the clearest possible results, the more sensitive position of (36, 36) is used.

The test results are shown in Fig. 7, where the x-axis is the pressure, and the y-axis is the maximum magnitude of the reconstructed conductivity variations. The blue line with round marks is that of the structure modality sensor, while the red line with squire marks is the data of the magnitude modality sensor. As the blue line shows, the reading of the structure modality sensor becomes stable after pressure increases to 100 kPa, meaning that the sensor reaches saturation state. The magnitude modality sensor starts to sense from 140 kPa and its conductivity still increases with the increasing pressure up to 200 kPa. This test validates that in the pressure range of 140 kPa to 200 kPa, the proposed multimodal sensor is effective.

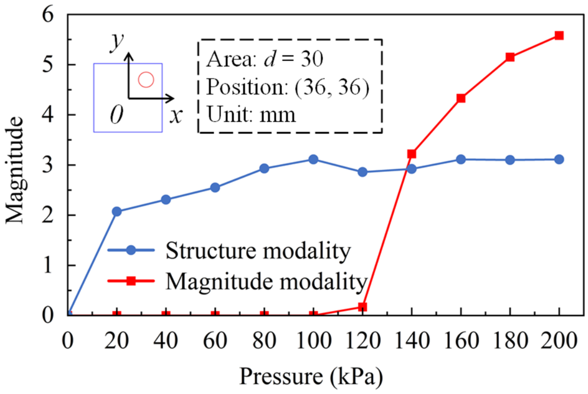

Fig. 7. Validation of the multimodal sensor. In the pressure range of 140 kPa to 200 kPa, the magnitude of structure modality sensor maintains constant, and that of magnitude modality sensor increase with increasing pressure. The mechanism of multimodal sensor is effective.

C. Single compressed area tests

In this test, two representative positions are selected as the centers of the compressed areas. One position is (0, 0), where the sensitivity is the lowest around all the sensing areas. The other is (36, 36), where the sensitivity is highest around all reachable test positions. Two circular indenters with different sizes (diameters of 30 mm and 40 mm) were used to apply pressure to the sensor. Four test cases are formed in total, with the permutation and combination of different sizes and positions of the indenters. To illustrate more clearly, a model is set for each case, as shown in Fig. 8. For each case, four pressures were applied, which are 140 kPa, 160 kPa, 180 kPa, and 200 kPa.

1) Pressure distribution images

The imaging results are shown in Fig. 8. In total, the multimodal CNN clearly reconstructs conductivity variation areas caused by pressure in all the cases and outperforms the other two algorithms. In case 1 and case 3, the compressed area is located at a low sensitivity position of (0, 0), and the reconstructed images using single modality CNN have distortion, while that of Tikhonov regularization are blurred. In case 2 and case 4, the compressed area is located at a high sensitivity position of (36, 36), all three methods can clearly reconstruct images. However, the blue area in Tikhonov imaging results is significantly larger than the red area, suggesting that the compressed area is not clearly segmented from the background. Two CNN enhanced algorithms clearly distinguish the boundary of the compressed areas. The reconstructed compressed area using single modality CNN is relatively smaller than the model in all the cases, while that of multimodal CNN is relatively larger when the diameter of compressed areas is 30 mm in cases 1 and 2.

In all cases, the reconstructed conductivity variation of $\Delta\hat{\boldsymbol{\sigma}}$ using multimodal CNN correctly reflects the variation of local pressure. With the pressure increasing, the color of the reconstructed image changes from yellow to deep red, which is consistent with the color bar at the bottom of the figure. The images reconstructed by Tikhonov regularization also show the pressure variations, but they are not clear in cases 1 and 3 of low sensitive area tests. The images of single modality CNN cannot show the pressure variation in cases 2 and 4.

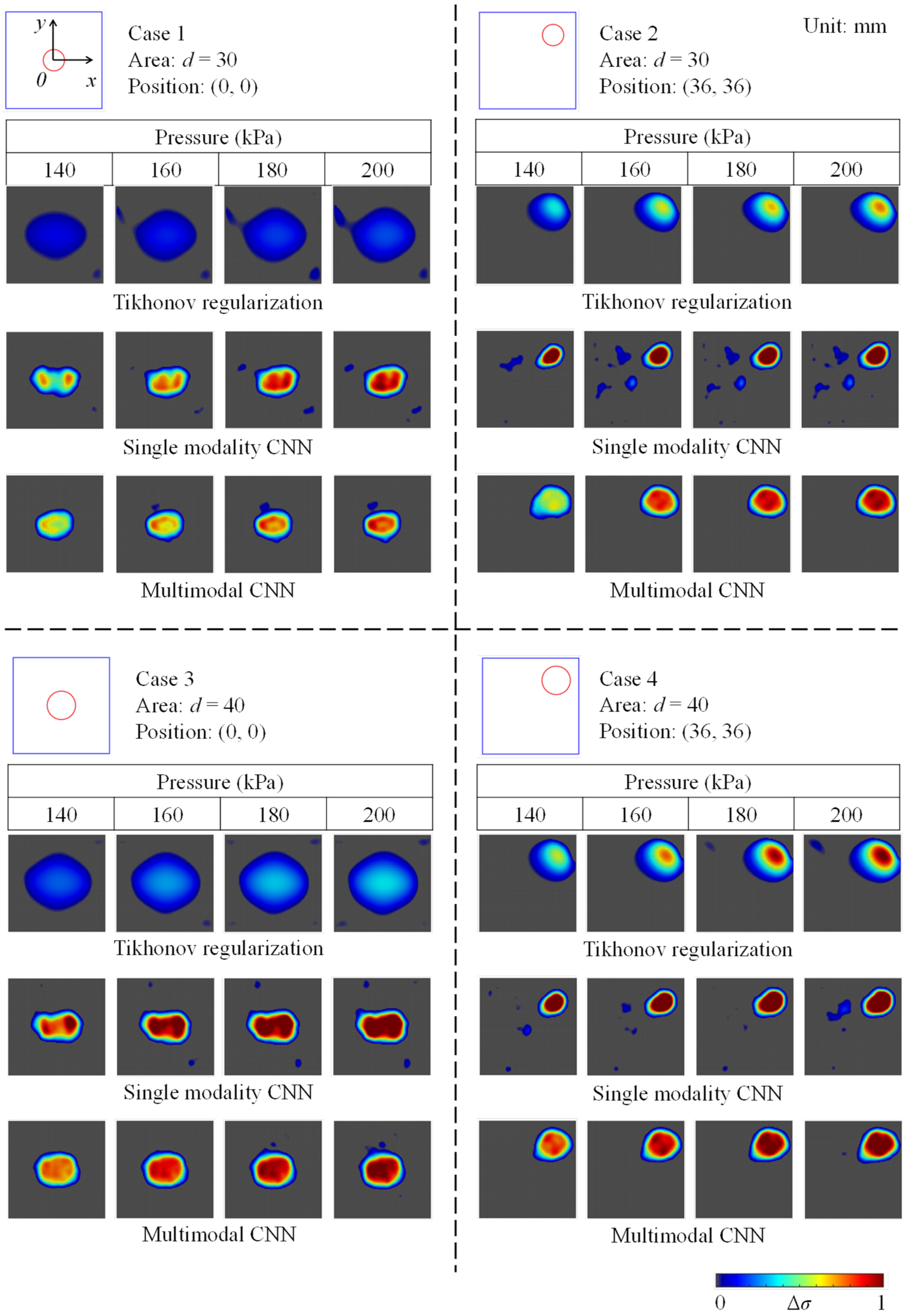

Fig. 8. Results of the single compressed area test. The diameter of the compressed areas is 30 mm in case 1 and 2, and 40 mm in case 3 and 4. For each case, four pressure of 140 kPa, 160 kPa, 180 kPa, and 200 kPa were applied. In all the cases, the multimodal CNN clearly reconstructs the geometry of compressed areas, as well as the conductivity variation caused by varying pressure, outperforms single modality CNN and Tikhonov regularization.

2) Pressure magnitude estimation

To show the pressure magnitude measurement more clearly, the data for images in Fig. 8 are reshaped into their vectors form by row and lined together in Fig. 9. In Fig. 9, the columns from the top to the bottom show the results of multimodal CNN, single modality CNN and Tikhonov regularization. Because Fig. 9 is the presentation of the data in Fig. 8 from different perspectives, the cases 1, 2, 3, and 4 in Fig. 9 are consistent with that in Fig. 8 respectively. The data in black, blue, green, and red are the reconstructed conductivity under the pressure of 140 kPa, 160 kPa, 180 kPa, and 200kPa respectively.

As results show, the magnitude of Tikhonov reconstructed $\Delta\hat{\sigma}$ increases with the increase of pressure, but in cases 1 and 3 (the compressed area is in the low sensitivity position), the magnitude of $\Delta\hat{\sigma}$ is significantly lower than that in cases 2 and 4 (high sensitivity position). This result clearly demonstrates that the uneven sensitivity of EIT sensors has significant impacts on magnitude detection. In the comparison of cases 1 and 3, with the same pressure, the bigger the compressed area, the higher the magnitude. This trend is also shown in the comparison between cases 2 and 4. The results show that the size of the compressed area also affected reconstructing the magnitude of $\Delta\hat{\sigma}$. Therefore, it is difficult to measure the magnitude solely using Tikhonov regularization and similar conventional algorithms.

The single modality CNN is not sufficient to rectify the impacts of uneven sensitivity and the varying compressed area sizes on the $\Delta\hat{\sigma}$ magnitude reconstruction, even though it is better than Tikhonov regularization. In cases 2 and 4, the magnitude of $\Delta\hat{\sigma}$ is not increased along with the pressure increase. Moreover, most of the reconstructed $\Delta\hat{\sigma}$ surpass 1, which does not consist with the condition that the input data of the CNN are processed with 0-1 normalization. It is also the reason why the color of the reconstructed compressed area using single modality CNN in Fig. 8 is the same as deep red, and not changing under different pressures.

The proposed multimodal CNN rectifies the impacts of the sizes of compressed areas and uneven sensitivity of the sensor, and its results basically reflect the pressure variation. In all cases, the reconstructed conductivity magnitude increases with increasing pressure. Comparing cases 1 and 2, where the size of the compressed area is the same, the magnitudes of the reconstructed conductivity are basically the same when the pressures are the same. The comparison between cases 3 and 4 also leads to the same conclusion. Comparing cases 1 and 3 (also cases 2 and 4), the multimodal CNN also corrects the influence of the size of compressed areas on the magnitude of reconstructed $\Delta\hat{\sigma}$.

To further understand the error of the three reconstruction methods, the magnitude of reconstructed $\Delta\hat{\sigma}$ are calculated in all cases under different pressures. The magnitude calculations method for three different reconstruction methods are slightly different. For the Tikhonov regularization, the maximum of the reconstructed $\Delta\hat{\sigma}$ is selected as the magnitude, because its reconstructed compressed areas are smooth but with blurred edges. The reconstruction results of single modality CNN and multimodal CNN have clear edges but lack smoothness, with discontinuous noise present. Therefore, for each reconstructed image of $\Delta\hat{\sigma}$, the threshold is set to 75% of the maximum value. Values exceeding this threshold are averaged to produce the final magnitude estimation.

Experimental settings of the cases (Unit: mm)

Case	Position	Diameter of the area
1	(0, 0)	30
2	(36, 36)	30
3	(0, 0)	40
4	(36, 36)	40

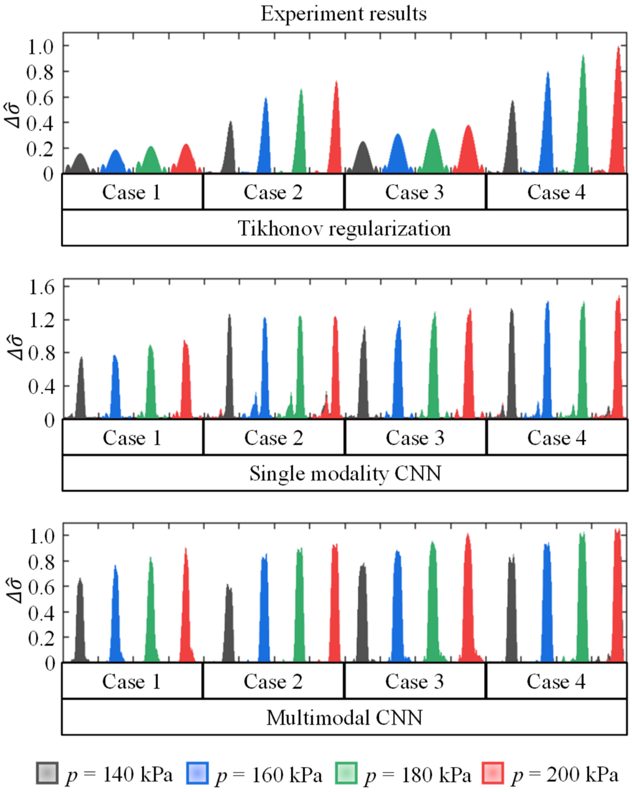

Fig. 9. Magnitude estimation in single compress area tests, the setting of the cases is the same as that in Fig. 8, with different colors representing different pressures. The multimodal CNN outperforms single modality CNN and Tikhonov regularization. Its magnitude reconstruction of $\Delta\hat{\sigma}$ reflects the pressure variation and is less impacted by the size of the compressed area and uneven sensitivity of the sensor.

For each pressure condition, the measurement error is calculated as the difference between the maximum and minimum magnitudes. The biggest error across all pressure conditions is considered as the error of the reconstruction method. When the pressure is 200 kPa, the amplitude estimated by Tikhonov regularization achieves the maximum error, which is 0.76. Since the data is 0-1 normalized, it can be considered that the error is 76% of the range of the sensor. The Single modality CNN achieves the maximum error of 57% when the pressure is 160 kPa, and the multimodal CNN reaches the maximum error of 21% when the pressure is 180 kPa. The results above show that the added structure modality effectively improves the accuracy of EIT sensors in pressure measurement. However, this result is still not satisfactory. Therefore, in future research, we will use more capable AI models to further improve the accuracy.

3) Localization validation

The localization accuracy of the sensor is validated. In this study, the indenter with a diameter of 30 mm was used to compress the sensor each time in different positions, and the distance between the centroid of the reconstructed compressed area and the indenter was calculated as a localization error. The image mass method in the reference [2] is adopted to evaluate the positions of the reconstructed compressed areas. In total, 25 evenly distributed positions have been tested. The distance between two adjacent positions is 18 mm along the x-axis and the y-axis. Each position was compressed with a constant pressure of 200 kPa. The results are shown in Fig. 10.

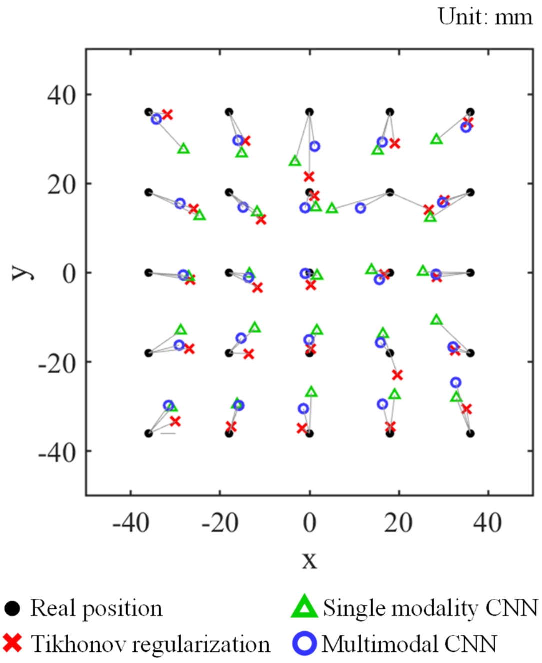

Fig. 10. Localization results of compressed areas with Tikhonov, single modality CNN, and multimodal CNN. As shown, the multimodal CNN (blue circles) outperforms the other two methods, reaching the localization error of $e_{\text{m-cnn}} = 6.4 \pm 5.5$ mm.

In Fig. 10, the black solid dots represent the true position of the indenter, and the red crosses, green triangles, and blue circles represent the estimated positions of the indenter obtained using the Tikhonov regularization, the single modality CNN and the multimodal respectively. The line segments connecting the marks demonstrate the correspondence between the estimated positions and their corresponding true positions. The figure shows that the positions estimated by three methods near the boundary of the sensor tend to be closer to the center. The multimodal CNN outperforms the other two method with localization error of $e_{m-cnn} = 6.4 \pm 5.5\, mm$, while that of the single modality CNN and the Tikhonov regularization are $e_{s-cnn} = 7.6 \pm 5.8\, mm$ and $e_{tik} = 7.7 \pm 6.6\, mm$, respectively. From all the experiments above, it can be inferred that the size of the compressed area has been effectively measured by the proposed multimodal EIT sensor when it is bigger than that of the indenter with diameter of 30 mm, which is approximately 4% of the total sensing area.

D. Multiple compressed areas tests

1) Pressure distribution images of two areas

The imaging results of the two compressed areas test are shown in Fig. 11, where Fig. 11 (a) is the reconstructed conductivity distribution images. Case 5 is used to evaluate the ability to reconstruct the compressed areas in different sensitivity positions. Both compressed areas have the same diameter of 30 mm, but area A1 is located at position (0, 0), which is the least sensitive position of the sensor, while area A2 is located at (36, 36), which has the highest sensitivity around all reachable test positions. Two different pressures of 140 kPa and 200 kPa were used for testing. For a clearer presentation, the hollow red legend in the models represents the area with 140 kPa pressure, and the solid red legend represents that with 200 kPa pressure.

As shown in Fig. 11 (a), multimodal CNN clearly distinguishes two compressed areas, and the sizes of the two reconstructed areas are almost identical, which is also consistent with the models. Meanwhile, the pressure variations are reflected in the reconstructed images. The high-pressure areas are in deep red, and the low-pressure areas are in light red. The results indicate that the multimodal CNN effectively rectifies the impact of different sensitivities on reconstructed images. Single modality CNN can clearly recognize areas in high sensitivity areas, but areas in low sensitivity areas have significant blurred fringes. The Tikhonov regularization is barely able to distinguish two compressed areas. The image of the compressed area in the low sensitive position is faded and merged into the fringe of that in the higher sensitive position.

Case 6 is used to evaluate the ability to reconstruct the compressed areas with different sizes. The larger compressed area of A_1 (diameter of 40 mm) and smaller area of A_2 (diameter of 30 mm) are located at (-36, -36) and (36, 36) respectively. Due to the symmetry of the sensors, the sensitivity of the two positions can be considered the same. As the figures show, the multimodal CNN still reconstructs the compressed area clearly, and the size difference of the compressed areas is distinguishable from the images. Meanwhile, the pressure changes are distinguishable from the reconstructed images. Single modality CNN also clearly reconstructs two areas, but the images are relatively smaller than the models, and pressure changes are also indicated in the images. Tikhonov regularization distinguishes two targets in this case, but the boundaries of the images are blurred.

2) Pressure magnitude estimation of two areas

To show the magnitudes of the reconstructed images in Fig. 11 (a) more clearly, the data of images are reshaped into their vectors form by row in Fig. 11 (b), which is similar to the figure pairs of Fig. 8 and Fig. 9. In Fig. 11 (b), p_1 and p_2 represent the pressure magnitudes of area A_1 and A_2 respectively, and the four colors represent the four combinations of p_1 and p_2. The reconstructed results using Tikhonov regularization and single modality CNN cannot indicate the pressure magnitudes. For the areas with smaller size or located in less sensitive positions, the reconstructed magnitude is always smaller than that of areas with larger size or in sensitive positions.

Multimodal CNN provides relatively decent reconstructions of the magnitudes in two compressed areas tests. In most tests of case 5 and case 6, the reconstructed magnitude of the high-pressure area is bigger than that of the low-pressure area, which is consistent with the pressure distribution settings of their models. The only exception is the extreme situations such as pressure combination with the black legend in case 5, where the area A_1 is located in the less sensitive region with high pressure of 200 kPa, and area A_2 is located in the sensitive region with low pressure of 140 kPa, but the reconstructed magnitude p_1 is only slightly higher than p_2.

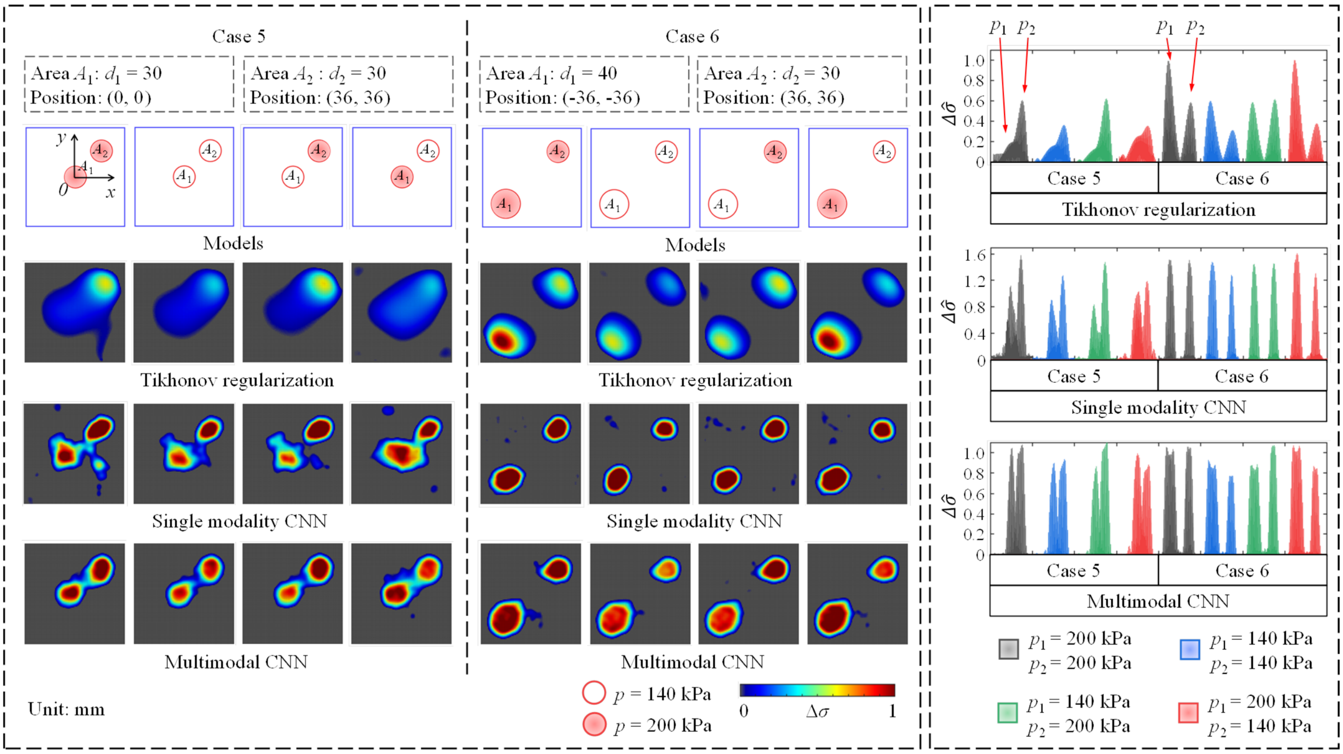

(a) (b)

Fig. 11. Two compressed areas test. (a) The imaging of the compressed areas. (b) The presentation of magnitude reconstruction in Fig.11 (a), p_1 is the pressure of area A_1, p_2 is the pressure on area A_2. The Multimodal CNN reconstructs clear images of the compressed areas in both cases, and distinguish different pressure magnitudes. The Single modality CNN can distinguish different compressed areas, but not pressure magnitudes. Tikhonov regularization barely distinguish two compressed areas in case 5.

3) Three and four areas tests

Fig. 12 shows the three and four compressed areas tests. Case 7 and case 8 show the measurement results of three compressed areas, while case 9 and case 10 show that of four compressed areas. Because the conductivity magnitudes reconstructed by the single modality CNN all exceed maximum range of (0, 1), we multiple them by 0.6 to better show the changes of magnitude in images. As shown in the figures, both CNN enhancement algorithms outperform Tikhonov regularization and clearly distinguish all compressed areas.

As for geometry reconstruction, the images using single modality CNN are relatively smaller than the models, the same as in the one and two compressed areas tests. Meanwhile, except in case 8, it is hard to distinguish the size differences of compressed areas very well from the images. multimodal CNN realizes a more decent geometry reconstruction of the compressed areas in cases 7, 8, and 10. The size differences are distinguishable and consistent with the models, except in case 9, where the overall measurement results are significantly larger than the model.

In terms of magnitude measurement, single modality CNN still barely distinguishes different magnitudes with different pressures. The accuracy of magnitude measurement by multimodal CNN decreases with the increased number of compressed areas. Except for fully compliant with the model in case 7, only partial of the magnitude of the compressed areas in the remaining cases comply with the models, such as areas A_1 and A_3 in case 8, areas A_1 and A_4 in case 10.

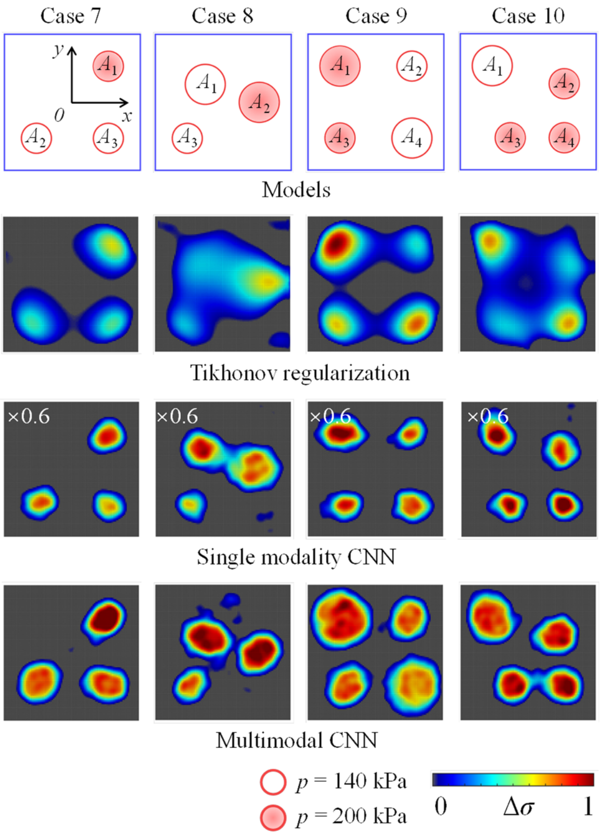

Fig. 12. The results of three and four compressed areas test. The single modality CNN and multimodal CNN are able to reconstruct the geometry of the compressed areas. The images of single modality CNN cannot indicate the pressure differences at all. The images of multimodal CNN still partially reflect the pressure differences, but not as reliable as in one and two areas tests.

VI. CONCLUSIONS:

In this study, a novel multimodal EIT sensor is proposed for pressure distribution measurement under complex pressure conditions. Compared with other single modal EIT pressure sensors, it contains an independent structural EIT pressure sensor, which provides extra structure information of the compressed areas as complements. A “two-step” multimodal CNN imaging method is designed to fuse two modalities of the multimodal EIT sensor. The simulation results show that adding extra modality does not reduce its robustness against noise, and improves its imaging accuracy in one and two conductivity varying areas tests compared to single modality CNN. The experimental results show that it effectively reconstructs the geometries of the compressed areas, and it is also a promising method for reconstructing pressure magnitude under complex pressure conditions.

One thing to be noted is that, as a cost of improving performance, adding an extra modality sensor increases the system complexity compared to a regular single modality EIT sensor. The structural complexity of the sensor is increased, because it is composed of two EIT sensors. The channel of the data acquisition device is also increased. Meanwhile, the simulation data for AI model training is also increased to simulate the extra structure modality sensor.

Our research on the AI model for multimodal fusion is still very preliminary, and still to be improved. Even though the multimodal AI (the baseline is CNN) used in the paper is able to validate the effectiveness of the proposed multimodal sensor, it is still not capable enough for complex cases. Especially the accuracy of measurements decreases with the increasing number of compressed areas. In the next step, we will try more capable AI models (such as Unet and ResNet), and develop a customized multimodal AI based on this paper to achieve better performances. Meanwhile, the imaging speed of the system needs to be improved. Even though the raw data acquisition speed of the device is 0.2 s for one image, but the entire tomography process is slowed down by the iterative PLS method to around 6 s. In our next step, it will be modified for higher speed.

ACKNOWLEDGMENT

Huaijin Chen and Zhanwei Wang are supported by China Scholarship Council (CSC) under NO. 202106830032 and NO. 202006080010.

Kevin Langlois is supported by a personal grant from the Wetenschappelijk Onderzoek (FWO) under grant 1258523N.

FWO SBO Sublime and the Flemish Government under the program Onderzoeksprogramma Artificiële Intelligentie (AI) Vlaanderen.

REFERENCES

[1] G. Pang, G. Yang, and Z. Pang, "Review of Robot Skin: A Potential Enabler for Safe Collaboration, Immersive Teleoperation, and Affective Interaction of Future Collaborative Robots," IEEE Transactions on Medical Robotics and Bionics, vol. 3, no. 3, pp. 681-700, 2021, doi: 10.1109/TMRB.2021.3097252.

[2] K. Park, H. Park, H. Lee, S. Park, and J. Kim, "An ERT-based Robotic Skin with Sparsely Distributed Electrodes: Structure, Fabrication, and DNN-based Signal Processing," in 2020 IEEE International Conference on Robotics and Automation (ICRA), 31 May-31 Aug. 2020 2020, pp. 1617-1624, doi: 10.1109/ICRA40945.2020.9197361.

[3] Y. J. Jeong, Y. E. Kim, K. J. Kim, E. J. Woo, and T. I. Oh, "Multilayered Fabric Pressure Sensor for Real-Time Piezo-Impedance Imaging of Pressure Distribution," IEEE Transactions on Instrumentation and Measurement, vol. 69, no. 2, pp. 565-572, 2020, doi: 10.1109/TIM.2019.2903701.

[4] D. Silvera-Tawil, D. Rye, M. Soleimani, and M. Velonaki, "Electrical Impedance Tomography for Artificial Sensitive Robotic Skin: A Review," IEEE Sensors Journal, vol. 15, no. 4, pp. 2001-2016, 2015, doi: 10.1109/JSEN.2014.2375346.

[5] Z. Cui, Y. Yu, and H. Wang, "Recent Developments in Impedance-Based Tactile Sensors: A Review," IEEE Sensors Journal, vol. 24, no. 3, pp. 2350-2366, 2024, doi: 10.1109/JSEN.2023.3339791.

[6] H. Alirezaei, A. Nagakubo, and Y. Kuniyoshi, "A highly stretchable tactile distribution sensor for smooth surfaced humanoids," in 2007 7th IEEE-RAS International Conference on Humanoid Robots, 29 Nov.-1 Dec. 2007 2007, pp. 167-173, doi: 10.1109/ICHR.2007.4813864.

[7] D. Silvera Tawil, D. Rye, and M. Velonaki, "Interpretation of the modality of touch on an artificial arm covered with an EIT-based sensitive skin," The International Journal of Robotics Research, vol. 31, no. 13, pp. 1627-1641, 2012/11/01 2012, doi: 10.1177/0278364912455441.

[8] D. Silvera-Tawil, D. Rye, and M. Velonaki, "Interpretation of Social Touch on an Artificial Arm Covered with an EIT-based Sensitive Skin," International Journal of Social Robotics, vol. 6, no. 4, pp. 489-505, 2014/11/01 2014, doi: 10.1007/s12369-013-0223-x.

[9] Y. Zhang, G. Laput, and C. Harrison, "Electrick: Low-Cost Touch Sensing Using Electric Field Tomography," presented at the Proceedings of the 2017 CHI Conference on Human Factors in Computing Systems, Denver, Colorado, USA, 2017. [Online]. Available: https://doi.org/10.1145/3025453.3025842.

[10] N. Biasi, A. Gargano, L. Arcarisi, N. Carbonaro, and A. Tognetti, "Physics-Based Simulation and Machine Learning for the Practical Implementation of EIT-Based Tactile Sensors," IEEE Sensors Journal, vol. 22, no. 5, pp. 4186-4196, 2022, doi: 10.1109/JSEN.2022.3144038.

[11] H. Chen, K. Langlois, J. Brancart, E. Roels, T. Verstraten, and B. Vanderborght, "A Novel Physical Human–Robot Interface With Pressure Distribution Measurement Based on Electrical Impedance Tomography," IEEE Sensors Journal, vol. 23, no. 18, pp. 21914-21923, 2023, doi: 10.1109/JSEN.2023.3303226.

[12] Y. Chen and H. Liu, "Location-Dependent Performance of Large-Area Piezoresistive Tactile Sensors Based on Electrical Impedance Tomography," IEEE Sensors Journal, vol. 21, no. 19, pp. 21622-21630, 2021, doi: 10.1109/JSEN.2021.3103988.

[13] H. Chen, X. Yang, J. Geng, G. Ma, and X. Wang, "A Skin-Like Hydrogel for Distributed Force Sensing Using an Electrical Impedance Tomography-Based Pseudo-Array Method," ACS Applied Electronic Materials, vol. 5, no. 3, pp. 1451-1460, 2023/03/28 2023, doi: 10.1021/acsaelm.2c01394.

[14] H. Chen, X. Yang, G. Ma, and X. Wang, "Correcting Non-Uniform Sensitivity in EIT Tactile Sensing via Jacobian Vector Approximation," IEEE Robotics and Automation Letters, vol. 9, no. 3, pp. 2335-2342, 2024, doi: 10.1109/LRA.2024.3355773.

[15] H. Park, H. Lee, K. Park, S. Mo, and J. Kim, "Deep Neural Network Approach in Electrical Impedance Tomography-based Real-time Soft Tactile Sensor," in 2019 IEEE/RSJ International Conference on Intelligent Robots and Systems (IROS), 3-8 Nov. 2019 2019, pp. 7447-7452, doi: 10.1109/IROS40897.2019.8968532.

[16] H. Park, K. Park, S. Mo, and J. Kim, "Deep Neural Network Based Electrical Impedance Tomographic Sensing Methodology for Large-Area Robotic Tactile Sensing," IEEE Transactions on Robotics, vol. 37, no. 5, pp. 1570-1583, 2021, doi: 10.1109/TRO.2021.3060342.

[17] H. Chen, X. Yang, P. Wang, J. Geng, G. Ma, and X. Wang, "A Large-Area Flexible Tactile Sensor for Multi-Touch and Force Detection Using Electrical Impedance Tomography," IEEE Sensors Journal, vol. 22, no. 7, pp. 7119-7129, 2022, doi: 10.1109/JSEN.2022.3155125.

[18] F. Behrad and M. Saniee Abadeh, "An overview of deep learning methods for multimodal medical data mining," Expert Systems with Applications, vol. 200, p. 117006, 2022/08/15/ 2022, doi: https://doi.org/10.1016/j.eswa.2022.117006.

[19] M. Sharma et al., "YOLOrs: Object Detection in Multimodal Remote Sensing Imagery," IEEE Journal of Selected Topics in Applied Earth Observations and Remote Sensing, vol. 14, pp. 1497-1508, 2021, doi: 10.1109/JSTARS.2020.3041316.

[20] Z. Wang et al., "Cross modality generative learning framework for anatomical transitive Magnetic Resonance Imaging (MRI) from Electrical Impedance Tomography (EIT) image," Computerized Medical Imaging and Graphics, vol. 108, p. 102272, 2023/09/01/ 2023, doi: https://doi.org/10.1016/j.compmedimag.2023.102272.

[21] Z. Liu, P. Bagnaninchi, and Y. Yang, "Impedance-Optical Dual-Modal Cell Culture Imaging With Learning-Based Information Fusion," IEEE Transactions on Medical Imaging, vol. 41, no. 4, pp. 983-996, 2022, doi: 10.1109/TMI.2021.3129739.

[22] Z. Liu and Y. Yang, "Multimodal Image Reconstruction of Electrical Impedance Tomography Using Kernel Method," IEEE Transactions on Instrumentation and Measurement, vol. 71, pp. 1-12, 2022, doi: 10.1109/TIM.2021.3132830.

[23] S. Ren, K. Sun, C. Tan, and F. Dong, "A Two-Stage Deep Learning Method for Robust Shape Reconstruction With Electrical Impedance Tomography," IEEE Transactions on Instrumentation and Measurement, vol. 69, no. 7, pp. 4887-4897, 2020, doi: 10.1109/TIM.2019.2954722.

[24] X. Zhang et al., "V-Shaped Dense Denoising Convolutional Neural Network for Electrical Impedance Tomography," IEEE Transactions on Instrumentation and Measurement, vol. 71, pp. 1-14, 2022, doi: 10.1109/TIM.2022.3166177.

[25] D. Liu, A. K. Khambampati, and J. Du, "A Parametric Level Set Method for Electrical Impedance Tomography," IEEE Transactions on Medical Imaging, vol. 37, no. 2, pp. 451-460, 2018, doi: 10.1109/TMI.2017.2756078.

[26] H. Lee, K. Park, J. Kim, and K. J. Kuchenbecker, "Piezoresistive textile layer and distributed electrode structure for soft whole-body tactile skin," Smart Materials and Structures, vol. 30, no. 8, p. 085036, 2021/07/13 2021, doi: 10.1088/1361-665X/ac0c2e.

[27] B. H. Brown and A. D. Seagar, "The Sheffield data collection system," Clinical Physics and Physiological Measurement, vol. 8, no. 4A, p. 91, 1987/11/01 1987, doi: 10.1088/0143-0815/8/4A/012.

[28] Y. Yang and J. Jia, "An Image Reconstruction Algorithm for Electrical Impedance Tomography Using Adaptive Group Sparsity Constraint," IEEE Transactions on Instrumentation and Measurement, vol. 66, no. 9, pp. 2295-2305, 2017, doi: 10.1109/TIM.2017.2701098.

[29] L. Yang, H. Wu, K. Liu, B. Chen, W. Han, and J. Yao, "Image Reconstruction Improvement With Optimal Driven-Measurement Pattern Selection for Electrical Impedance Tomography," IEEE Sensors Journal, vol. 21, no. 12, pp. 13530-13539, 2021, doi: 10.1109/JSEN.2021.3068460.

[30] Y. Yang and L. Peng, "Data Pattern With ECT Sensor and Its Impact on Image Reconstruction," IEEE Sensors Journal, vol. 13, no. 5, pp. 1582-1593, 2013, doi: 10.1109/JSEN.2013.2237763.

[31] M. Vauhkonen, D. Vadasz, P. A. Karjalainen, E. Somersalo, and J. P. Kaipio, "Tikhonov regularization and prior information in electrical impedance tomography," IEEE Transactions on Medical Imaging, vol. 17, no. 2, pp. 285-293, 1998, doi: 10.1109/42.700740.

[32] D. Liu, D. Smyl, and J. Du, "A Parametric Level Set-Based Approach to Difference Imaging in Electrical Impedance Tomography," IEEE Transactions on Medical Imaging, vol. 38, no. 1, pp. 145-155, 2019, doi: 10.1109/TMI.2018.2857839.

[33] Y. Wu, B. Chen, K. Liu, T. Zhou, G. Gao, and J. Yao, "An adaptive parametric level-set method for lung health monitoring with smartphone-based electrical impedance tomography," Measurement Science and Technology, vol. 33, no. 9, p. 095403, 2022/06/22 2022, doi: 10.1088/1361-6501/ac769c.

[34] A. Kadu, T. v. Leeuwen, and W. A. Mulder, "Salt Reconstruction in Full-Waveform Inversion With a Parametric Level-Set Method," IEEE Transactions on Computational Imaging, vol. 3, no. 2, pp. 305-315, 2017, doi: 10.1109/TCI.2016.2640761.

[35] D. Liu, Y. Zhao, A. K. Khambampati, A. Seppänen, and J. Du, "A Parametric Level set Method for Imaging Multiphase Conductivity Using Electrical Impedance Tomography," IEEE Transactions on Computational Imaging, vol. 4, no. 4, pp. 552-561, 2018, doi: 10.1109/TCI.2018.2863038.

Huaijin Chen, received the B.E. and M.Sc. degree from Nanjing University of Aeronautics & Astronautics (NUAA), Nanjing, China, in 2018 and 2021 respectively. He is currently a Ph.D. student in Vrije Universiteit Brussel (VUB), Brussels, Belgium. His research interests are mainly about electrical impedance tomography pressure sensor.

Zhanwei Wang, received the BEng and MEng degrees in the Department of Mechanical Engineering at Northeastern University, China in 2017 and 2020 respectively. He is now a PhD student at Brubotics at the Vrije Universiteit Brussels and is affiliated with Imec. He is funded by China Scholarship Council(CSC), with grant number 202006080010. His research focuses on self-healing and soft robotics, including soft actuators, intelligent responsive structures, and soft matter simulations.

Kevin Langlois, received the degree of Doctor of Engineering Sciences at the Vrije Universiteit Brussel (VUB), Brussels, Belgium in 2022. The focus of his research is on safe, comfortable, and efficient human-robot interactions. He is currently a post-doctoral researcher supported by the FWO and affiliated to imec. His research interests include sensors for physical human-robot interfaces and rehabilitation robotics.

Tom Verstraten, received his Ph.D. from Vrije Universiteit Brussel (VUB) in 2018. He was appointed as assistant professor at the Robotics & Multibody Mechanics Research Group (R&MM) of the VUB in 2020. He was awarded fellowships of the FWO for both his doctoral and postdoctoral research, as well as a Fulbright grant for visiting scholars for a research stay at the University of Tulsa (United States) in 2018-19. He also worked in industry as a R&D Engineer at Aquasystems International (2012-13) and as a visiting researcher at TU Darmstadt (Germany) in 2017. His main research focus is the study and development of energy-efficient actuation systems for robotic prostheses, exoskeletons and collaborative robots. Research interests include elastic actuators and redundant actuation.

Bram Vanderborght, received his PhD from the Vrije Universiteit Brussel in 2007. He performed research at JRL lab in AIST, Tsukuba (Japan) and did his post-doc researcher at the Italian Institute of Technology. Since 2009 he is professor at the VUB. He had an ERC starting grant and is currently coordinating three EU projects on smart and self-healing materials for soft robots. His research interests are human-robot collaboration for applications for health and manufacturing like exoskeletons, prostheses, social robots, drones and cobots. He is affiliated to the Interuniversity Microelectronics Institute (imec), Belgium, as scientific collaborator.